Theory for all-optical responses in topological materials: The velocity gauge picture

Dasol Kim [1,2] Dongbin Shin [3,4] Alexandra S. Landsman,[2,5] Dong Eon Kim,[1,2,*] and Alexis Chacón [1,2,†]

[1]*Department of Physics and Center for Attosecond Science and Technology, POSTECH, 7 Pohang 37673, South Korea*
[2]*Max Planck POSTECH/KOREA Research Initiative, Pohang 37673, South Korea*
[3]*Max Planck Institute for the Structure and Dynamics of Matter and Center for Free Electron Laser Science, 22761 Hamburg, Germany*
[4]*Department of Physics and Photon Science, Gwangju Institute of Science and Technology (GIST), Gwangju 61005, Republic of Korea*
[5]*Department of Physics, Ohio State University, 191 West Woodruff Ave, Columbus, Ohio 43210, USA*

High-order harmonic generation (HHG), which has been widely studied in atomic gas, has recently been expanded to solids to study the highly nonlinear electronic response in condensed matter and produce coherent high-frequency radiation. Recently, attention has turned to topological materials and the use of HHG to characterize topological bands and invariants. However, the theoretical interpretation of the nonlinear electronic response in topological materials presents many challenges. In particular, the Bloch wavefunction phase of topological materials has undefined points in the Brillouin zone. This leads to singularities in the calculation of the interband and intraband transition dipole matrix elements of the semiconductor Bloch equations (SBEs). Here, we use the laser-electromagnetic velocity gauge $\boldsymbol{p} \cdot \mathbf{A}(t)$ to numerically integrate the SBEs and treat the singularity in the production of the electrical currents and HHG spectra with better numerical efficiency and more straightforward implementation. We used a prototype of Chern insulators (CIs), the Haldane model, to demonstrate our approach. The validity of the velocity gauge approach is demonstrated in the following way: for topologically trivial materials such as MoS_2, qualitative agreement is achieved with the results of the length gauge approach and the time-dependent density functional theory. For the application of the velocity gauge approach to topological materials, Chern insulator is taken, using the two-band Haldane model. We found a good qualitative agreement between the velocity gauge and the length gauge approach in view of (i) the selection rules, (ii) the linear cutoff law scaling, and (iii) anomalous circular dichroism. We conclude that the velocity-gauge approach for HHG provides a theoretical tool to investigate topological materials.

I. INTRODUCTION

The measurement of the quantum spin Hall effect (QSHE) [1–5] in HgTe (2007) ushered in a new era of condensed matter physics, paving the way for unexpected technological advances [3,6,7]. The HgTe material consists of quantum wells that exhibit transverse spin currents at the edge, but insulating features in the bulk under a static longitudinal voltage [6,8] (see Fig. 1). These edge currents and insulating bulk suggest unique applications for a topological insulator (TI) in metrology [9] and in the control of quantum logic operations [10].

The quantum wells of HgTe, as well as other materials such as CdTe [2], have topological invariants belonging to the class $\mathbb{Z}_2$ of TI. This topological invariant is defined in terms of the wavefunction parities or Berry phase [2,6]. The two-dimensional (three-dimensional) TI is a unique phase of matter in the sense that the edge (surface) current is protected by the *time-reversal symmetry* of the Hamiltonian [11]. For edge states, this symmetry provides robustness against localization and forbids backscattering between states of opposite spin and opposite momentum [6].

Despite widespread interest in the nonlinear interaction of topological materials with ultrafast laser pulses, there is little research on the topic because of the difficulties in theoretical modeling and interpretation of resulting high-order harmonic emission. Addressing these challenges is instrumental in guiding future experimental observations in topological materials. In this paper, we focus on the study of nonlinear optical emission to topological materials by solving the semiconductor Bloch equations (SBEs) in the laser-electromagnetic velocity gauge (VG) $\boldsymbol{p} \cdot \mathbf{A}(t)$ in the mid-infrared (MIR) spectral regime. In particular, we introduce a new approach to address the integration of singularity in the SBEs for the highly nonlinear optical response in the topological materials.

There is a wide variety of topological materials depending on the *topological invariant* and the Hamiltonian symmetries of these materials. These classifications are organized in the periodic table of topological materials (insulators), shown in Ref. [6]. Depending on the dimensionality of the samples, symmetries, and topological invariant, this table shows topological materials with charge currents, locked-spin up and down currents [12,13], and Weyl fermions, among others. For instance, QSHE leads to quantum spin hall insulators (QSHI) HgTe (two-dimensional TI) or Bi_2Se_3 (three-dimensional TI).

In 1988, Haldane introduced the first paradigmatic class of topological materials showing quantum anomalous Hall

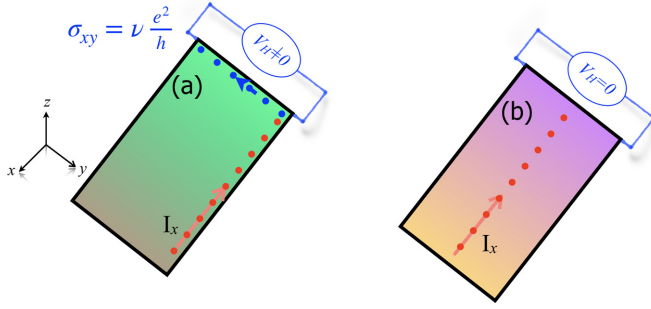*kimd@postech.ac.kr
†achacon@postech.ac.kr

FIG. 1. Quantum anomalous Hall effect. Panel (a) depicts a path of the longitudinal electrical currents I_x (red dots) and the *quantized transversal conductivity* $\sigma_{xy} = \nu \frac{e^2}{h}$ (Hall voltage $V_H \neq 0$ or charge current in blue dots) in an ideal Chern insulator (CI) proposed by Haldane [13] (the Chern number or topological invariant can be $\nu = \pm 1$), i.e., the quantum Hall effect without any applied external magnetic field. Panel (b) shows an example of traditional conductors, which do not exhibit any quantized transversal Hall voltage ($V_H = 0$ or conductivity), $\nu = 0$.

effects (QAHEs) (see Appendix A). The Haldane model exhibits *quantized conductivities*, $\sigma_{xy} = \nu \frac{e^2}{h}$ at the edge, where e is the electron charge, h is the Planck constant, and ν is the topological invariant (or the Chern number). This invariant is a quantized integer number that characterizes topological Chern insulators (CIs) (see Fig. 1). Topological states have *singularities* in the Brillouin zone (BZ), which can lead to numerical problems (see Fig. 12 in Appendix B or Fig. 2 of Ref. [14]). Here, we treat these *singularities* by using the VG approach. As a proof of concept, we use the Haldane model for CI to test and validate this approach.

Figure 1(a) depicts the quantum Hall effect (QHE) without Landau levels [6,13,15]. This shows that ν is essential for topological materials. Moreover, this critical aspect of topological materials is contained in the undefined phase of the topological states. The singularity itself is independent of the wavefunction gauge $|\tilde{u}_m^s\rangle = \exp(i\phi_m)|\tilde{u}_m^s\rangle$: the **k** position of the singular point can be manipulated via the gauge transformations, but not eliminated in topological materials. The latter leads to an interconnection of the singularity in the wavefunction phase with ν [16]. Kohmoto showed that *without this singularity, no* QHE *is observed* [16] and the material behaves as an ordinary semiconductor or conductor [see Fig. 1(b)]. Unfortunately, this singularity of the wavefunction affects the calculation of the Chern number, which is defined by [6,12,13,15]

$$\nu_m = \frac{1}{2\pi} \int_{\text{BZ}} d^2\mathbf{k} \cdot \boldsymbol{\Omega}_m(\mathbf{k}), \tag{1}$$

where $\boldsymbol{\Omega}_m(\mathbf{k}) = \langle \partial_{\mathbf{k}} u_{m,\mathbf{k}}| \times |\partial_{\mathbf{k}} u_{m,\mathbf{k}}\rangle = \nabla_{\mathbf{k}} \times \boldsymbol{\xi}_m(\mathbf{k})$ is the Berry curvature, $\boldsymbol{\xi}_m(\mathbf{k}) = i\langle u_{m,\mathbf{k}}|\nabla_{\mathbf{k}} u_{m,\mathbf{k}}\rangle$ is the Berry connection, and $\boldsymbol{d}_{mn}(\mathbf{k}) = i\langle u_{m,\mathbf{k}}|\nabla_{\mathbf{k}} u_{n,\mathbf{k}}\rangle$ are the transition dipole matrix elements. This singularity extremely complicates the calculations of the dipoles and Berry connections, see Ref. [14] and Fig. 2(a) in comparison to Fig. 2(b).

On the other hand, the ultrafast nonlinear optical spectroscopy and high-order harmonic generation (HHG) in
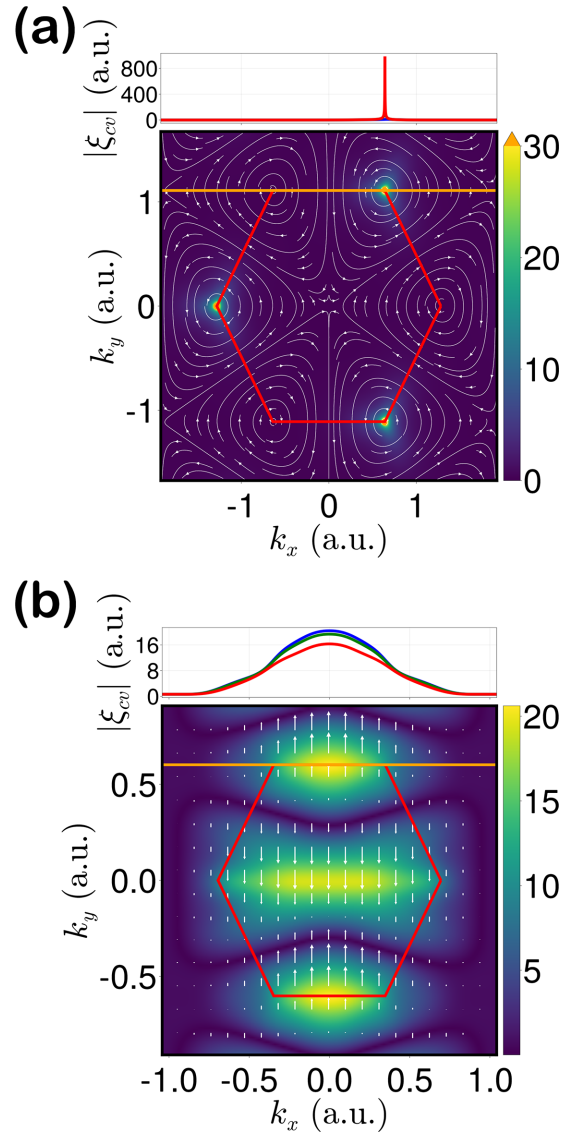

FIG. 2. Singularity in the Berry connection of topological material. The absolute value of the Berry Connection for (a) a Chern insulator defined in the topological Haldane model and (b) a topologically trivial material, MoS$_2$. The vectorial field indicates how the Berry connection can accumulate a phase in the Brillouin zone. In other words, by the Stokes' theorem, the topological Chern number is $\nu_n = \frac{1}{2\pi} \oint_C \boldsymbol{\xi}_n(\mathbf{k}) \cdot d\mathbf{k}$, where C denotes a closed line-path integral. The upper panels show a 1D cross section along the orange line with slightly varying k_y for trivial and topological phase, i.e., the absolute value of the Berry connection for small k_y offsets, respectively.

topological materials have drawn the attention of ultrafast physics and condensed matter communities [17,18] as a complementary alternative to angle-resolved photoelectron measurements [17,17,19,20]. However, the use of HHG to characterize topological materials is still in its infancy. How *topological invariants* are encoded in the HHG spectrum is yet to be explored. A few recent studies of HHG using the paradigmatic Haldane model [17,21] have shown the complexity of computing the nonlinear currents using the SBEs.

The evolutionary density matrix $\hat{\rho}(\mathbf{K}, t)$ or the semiconductor Bloch equations (SBEs) reads

$$\frac{\partial}{\partial t}\hat{\rho}_{mn}(\mathbf{K}, t) = -i\left[\varepsilon_{mn}(\mathbf{K} + \mathbf{A}(t)) - i\frac{1 - \delta_{m,n}}{T_2}\right]\hat{\rho}_{mn}(\mathbf{K}, t)$$
$$- i\mathbf{E}(t) \cdot [D(\mathbf{K} + \mathbf{A}(t)), \hat{\rho}(\mathbf{K}, t)]_{mn}. \quad (2)$$

The above equation contains the singular term of the topological wavefunction: the Berry connection and the dipole matrix element that are encoded in $D_{mn}(\boldsymbol{k})$ [14] (see Appendix A for mathematical definition). This $D_{mn}(\boldsymbol{k})$ contains both the interband dipole matrix element $\mathbf{d}_{mn}(\boldsymbol{k})$ for $m \neq n$ and the intraband Berry connection $\boldsymbol{\xi}_m(\boldsymbol{k})$ for $m = n$. Here $\mathbf{A}(t) = -\int_{t_0}^{t} \boldsymbol{E}(t')dt'$ is the vector potential of the electric field $\mathbf{E}(t)$, and $\varepsilon_{mn}(\boldsymbol{k}) = \varepsilon_m(\boldsymbol{k}) - \varepsilon_n(\boldsymbol{k})$ is the energy difference between the mth and nth bands. We use the so-called moving BZ frame [22], $\boldsymbol{k} = \mathbf{K} + \mathbf{A}(t)$, and the phenomenological dephasing time T_2 as in previous works [22–26]. For relaxation, we consider only the dephasing time of coherence T_2 [22,24]. Relaxation of the population is ignored due to its longer time scale compared to T_2. If the singularities in $D_{mn}(\boldsymbol{k})$ in Eq. (2) are not handled properly, it induces numerical errors in the calculation of HHG from topological materials, which is more noticeable in strong field regimes. These lead to *incorrect plateau* and *cutoff structures* of the HHG spectra (see Appendix B).

To address this problem, we previously developed the variable "matter-gauge wavefunctions" method [approach (*a*)], which considers the pseudospin gauge Hamiltonian and the periodicity of the Haldane model in the BZ [14]. This approach showed an excellent resolution of the harmonic orders (HOs) and cutoff of the HHG spectra. Additionally, the theoretical efforts of Silva *et al.* [27] dealt with this singularity by using the time evolution of $\hat{\rho}(\boldsymbol{k}, t)$ in the maximally localized Wannier basis (MLWB) [approach (*b*)]. Note that we have verified that both approaches (*a*) and (*b*) reach the same results in the Hamiltonian Bloch basis [14].

Each approach, (*a*) or (*b*), has its advantages and disadvantages. For instance, in [14], the approach (*a*) only works in the special case of tight binding approximations (TBAs). In [27], the approach (*b*) requires additional computational power to apply the dephasing time at each time step. (See Appendix C for more details.) The MLWB approach requires evaluations of T_2 in the Hamiltonian gauge instead of its original Wannier gauge representation, resulting in an increased number of computational operations and a more complex implementation.

To treat the singularity problem alternatively in topological materials and give another physical interpretation, we focus ourselves on the VG to solve the SBEs and compute the electrical currents in trivial materials and topological materials. Furthermore, we compare the HHG spectra produced by the proposed VG SBEs with those of the length gauge (LG) SBEs. The rest of the paper is organized as follows: In Sec. II, we describe the electrical current and the SBEs in the LG and VG. In Sec III, we use the VG SBEs to calculate HHG emission from trivial material such as a monolayer of MoS₂. We compare these results with those of the LG SBEs and the time-dependent density functional theory (TDDFT) for MoS₂, to confirm the validity of our approach. We then extend

the application of the proposed VG theoretical framework to topological CIs for both linearly and circularly polarized MIR or THz light sources. Our approach is further validated by computing the cutoff law [28] of the HHG spectra and the circular dichroism (CD) in topological materials. We also compare these outcomes with the LG results. In Sec. IV, we discuss the advantages and disadvantages of the LG and VG approaches in computing the HHG spectra and conclude that the VG approach is a suitable and straightforward method to calculate the HHG spectra for topological materials.

II. THEORETICAL FRAMEWORK

In the dipole approximation, VG and LG are theoretically used to describe the nonlinear optical responses [29–31] in solids subject to ultrashort lasers. The total Hamiltonian of the laser-lattice system is $\hat{H}(t) = \hat{H}_0 + \hat{V}_{\text{int}}(t)$, and the interaction term $\hat{V}_{\text{int}}(t)$ in the VG or LG reads

$$\hat{V}_{\text{int}}^{(\text{VG})} = \hat{\boldsymbol{p}} \cdot \mathbf{A}(t) + \mathbf{A}^2(t)/2, \text{ and} \quad (3)$$

$$\hat{V}_{\text{int}}^{(\text{LG})} = \hat{\boldsymbol{x}} \cdot \mathbf{E}(t). \quad (4)$$

Although these laser-electromagnetic gauges should provide the same results for a physical observable, for instance, the HHG spectra, previous studies have found that, unfortunately, it is not the case in several systems [31–33]. This breaking of the gauge symmetry occurs when an approximation is carried out to solve the time-dependent Schrödinger equation (TDSE). Note, however, that the full numerical integration of the TDSE for the HHG spectra under the LG and VG is covariant [34,35]. This supports the observation that some approximations of the TDSE can break the laser-electromagnetic gauge symmetry. For instance, in the strong field approximation (SFA) applied to a gas, this laser-electromagnetic gauge symmetry is broken [36], and produces different HHG spectra, particularly for the intensity yield [32,33]. Nevertheless, the main qualitative features of the HHG spectra are reproduced by both the LG and VG in the SFA formalism. In the case of topological materials, we expect a similar trend.

In the LG, the numerical integration of the SBEs is an extremely problematic task: The $\boldsymbol{k}$-space position operator depends on the crystalline momentum derivatives $\partial_{\boldsymbol{k}}$ in the BZ [see Eq. (10)]. Therefore, a discontinuous wavefunction gauge leads to a singularity in the derivative. Even in trivial materials, it is a numerical challenge to find a smooth wave function gauge that has no discontinuity and, therefore, does not give the singularity in derivatives $\partial_{\boldsymbol{k}}$ [24]. In topological materials, this is more critical since the discontinuity is not avoidable.

In contrast, the VG offers a way to avoid the singularity by decoupling of the different $\boldsymbol{k}$ channels. Hence, notwithstanding some disadvantages of the VG, related to the Bloch acceleration theorems [29–31] and crystal kinetic momenta, the VG offers an attractive alternative to the LG. Therefore, we propose the VG as an alternative to the LG to study the nonlinear optical responses of topological materials.

A. Velocity gauge picture

Frequently, in a periodic crystalline structure under external laser fields, the charge current is calculated by integrating the k-elementary-microscopic currents in the BZ,

$$J(t) = \int_{\mathrm{BZ}} \frac{d^3k}{(2\pi)^3} j(k, t). \tag{5}$$

Here, we define the elementary microscopic current $j(k, t)$ in the VG as

$$
\begin{aligned}
j(k, t) &= -\mathrm{Tr}(\hat{\rho}\hat{v}) \\
&= \mathrm{Tr}(\rho(k, t)\hat{p}) - N_{\mathrm{VB}}A(t) \\
&= -\sum_{m,n} \rho_{mn}(k, t)P_{nm}(k) - N_{\mathrm{VB}}A(t). \tag{6}
\end{aligned}
$$

This corresponds to the expectation value of the *velocity operator* $\hat{v} = -i[\hat{H}(t), \hat{x}]$. The current $j(k, t)$ is defined in terms of the density matrix $\hat{\rho} = \hat{\rho}(k, t)$, the momentum matrix element P, and the number of valence band N_{VB} [24,30,31].

The time-propagation of the density matrix $\hat{\rho}(k, t)$ is given by the Liouville-von Neumann equation,

$$i\frac{\partial \hat{\rho}(k, t)}{\partial t} = [\hat{H}(t), \hat{\rho}(k, t)], \tag{7}$$

where $\hat{\rho}$ will be evaluated in the VG via $\hat{H}(t)$.

Usually, the Hamiltonian representation is defined by the Bloch states for the laser-free Hamiltonian, $\hat{H}_0$. In the VG, the Hamiltonian describing the laser-periodic crystalline interaction reads

$$\hat{H}(t) = \hat{H}_0 + \hat{p} \cdot \mathbf{A}(t) + A^2(t)/2. \tag{8}$$

However, the term proportional to $A^2(t)$ is canceled by the commutator in the Liouville-von Neumann equation given by Eq. (3) [37]. Thus, the time evolution of the density matrix elements in the VG reads

$$
\begin{aligned}
\dot{\rho}_{mn}(k, t) = &-i\left[\varepsilon_{mn}(k) - i\frac{1 - \delta_{m,n}}{T_2}\right]\rho_{mn}(k, t) \\
&- iA(t) \cdot \sum_l [P_{ml}(k)\rho_{ln}(k, t) - P_{ln}(k)\rho_{ml}(k, t)]. \tag{9}
\end{aligned}
$$

Here $\varepsilon_{mn}(k)$ is the energy difference between bands m and n, with the phenomenological dephasing time given by T_2.

The advantage of the VG is that every k-crystal momentum channel is decoupled [30,31]. Therefore, the singularity from discontinuous phase of Bloch function can be avoided. Also, the VG SBEs does not have a Berry connection term, which is another source of singularity. Furthermore, we can quickly parallelize the implementation of the code for Eq. (9). For example, we use the message passing interface (MPI) in C + + and numerically solve Eq. (9) using the Runge-Kutta fifth-order method.

B. Length gauge pictures

The evolution of the electronic density operator $\dot{\hat{\rho}}(k, t)$ in LG and the "Hamiltonian matter gauge" can be acquired in a similar procedure as described in Refs. [14,30,31]. From

the Liouville-von Neumann equation given by Eq. (7), considering the interacting potential of Eq. (4) and the position operator in the Bloch basis $\hat{x}$ [38],

$$\hat{x}_{mn} = (-i\nabla_k + \xi_m)\delta_{mn} + d_{mn}, \tag{10}$$

$\dot{\hat{\rho}}(k, t)$ can be expressed as Eq. (2). This representation is sensitive to the singularity of the topological states in topological materials, as discussed above. The position operator indeed contains intraband momentum terms, which are defined in ∇_k. In a finite and discrete k-space grid, this means that $\hat{\rho}(k, t)$ depends on its k-space "numerical neighbor cell" and the electric field strength. This is problematic in LG and in its Hamiltonian representation. Even in the case that one can express the time evolution of $\hat{\rho}(K, t)$ in terms of the moving frame $k = K + \mathbf{A}(t)$ [14,22,39], the vector potential $\mathbf{A}(t)$ will force $\hat{\rho}(K, t)$ to travel throughout the singularity described in Fig. 2(a) for topological materials.

The numerical solution to Eq. (2) requires continuous quantities such as transition dipole matrix elements and Berry connections. Unfortunately, this is not possible for topological materials [14,16]. The Wannier representation [27] promises to address this problem. From the application of Eq. (7), considering TBA as a basis and Eq. (2), the equation of motion of density matrix in the Wannier basis yields [27]

$$
\begin{aligned}
i\frac{\partial}{\partial t}\hat{\rho}^{(\mathrm{W})}(K, t) = &\left[\hat{H}_0^{(\mathrm{W})}(K + A(t)), \hat{\rho}^{(\mathrm{W})}(K, t)\right] \\
&+ \mathbf{E}(t) \cdot [D^{(\mathrm{W})}(K + A(t)), \hat{\rho}^{(\mathrm{W})}(K, t)]. \tag{11}
\end{aligned}
$$

Here, $\hat{H}_0^{(\mathrm{W})}(k)$ is expressed in the TBA Hamiltonian. $D^{(\mathrm{W})}(k)$ and $\hat{\rho}^{(\mathrm{W})}(k, t)$ are dipole matrix and density matrix in Wannier basis. $D^{(\mathrm{W})}(k)$ is calculated by

$$D_{nm}^{(\mathrm{W})}(k) = \sum_R e^{ik \cdot R} \langle 0n|\hat{r}|Rm\rangle. \tag{12}$$

This exhibits continuous dipoles even in the case of topological materials. Furthermore, if we assume that $D^{(\mathrm{W})}(k)$ is diagonal, for instance,

$$\langle 0n|\hat{r}|Rm\rangle = \delta_{0R}\delta_{nm}\Delta_n, \tag{13}$$

one can treat $D^{(\mathrm{W})}(k)$ as a k-independent term [40]. Here $\Delta_n = \langle 0n|\hat{r}|0n\rangle$ is the center of nth Wannier function or can be understood as a position of the corresponding atomic orbital.

III. NUMERICAL RESULTS AND VALIDATIONS

A. Nonlinear optical response in trivial materials: The velocity gauge

Our VG SBEs are first validated in a topologically trivial material. Subsequently, we extended the VG SBEs to the paradigmatic Haldane model. In the case of trivial materials, we calculated the HHG spectra using both the LG SBEs and the TDDFT [41] for comparison with the results of the VG SBEs. For a trivial material, we use a simplified three-band TBA for monolayer MoS_2 from the study of Liu *et al.* [42]. This model only uses Mo-d_{z^2}, d_{xy}, and $d_{x^2-y^2}$ orbitals and includes the interaction between Mo-d orbital and the S-p orbital as an approximation. We simulate the HHG spectrum using VG and LG via Eqs. (9) and (11), respectively.
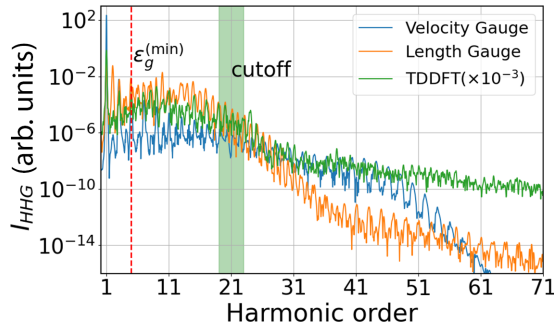
FIG. 3. Calculated HHG spectra from MoS_2 by the SBEs in the length gauge (orange line), velocity gauge (blue line) and TDDFT (green line). Our laser parameters are $\hbar\omega_0 = 0.3626$ eV, peak electric field $E_0 = 0.01265$ a.u. and time pulse duration at full width at half maximum (FWHM) of 14 opt. cycles under a gaussian envelope, with dephasing time $T_2 = 2.7$ fs. We used the tight binding model and parameters from the study of Liu *et al.* [42]. The red-dotted line indicates the band gap of the MoS_2, which is 1.8 eV.
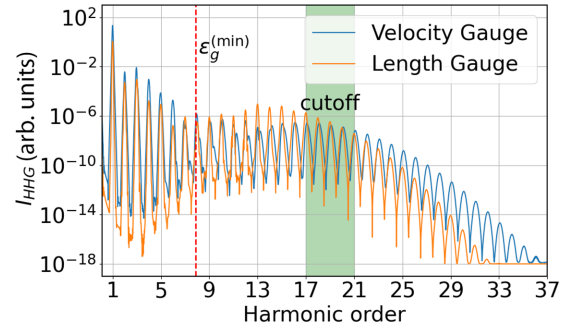

FIG. 4. Calculated HHG spectra from Chern insulator in the length and velocity gauges. Laser central frequency $\omega_0 = 0.38$ eV, peak electric field $E_0 = 0.0045$ a.u. and FWHM duration of 14 cycles under a gaussian envelope are used. For dephasing time $T_2 = 5.3$ fs is used. The Chern insulator has $M_0 = 0.0635$ a.u., $t_1 = 0.075$ a.u., $t_2 = 0.025$ a.u., and $\phi_0 = 1.16$ rad for Haldane model parameters. The red dotted line indicates the band gap of material, which is 3.0 eV.

Figure 3 shows HHG signals for both gauges in the trivial material, MoS_2. The spectrum produced by the VG SBEs share essential features to the LG and the TDDFT calculations. For example, the plateau with even and odd HO structures and the cutoff in the HHG spectra from the VG SBEs are qualitatively in good agreement with the other two methods. For better visualization, the TDDFT calculation is normalized to have similar low-order harmonics yields.

The LG and VG will yield identical results [43], if and only if the full eigenstates and eigenenergies of the Hamiltonian $H_0^{(W)}$ are considered in the simulation and the sum rule in Appendix D is satisfied. Moreover, since we use TBA up to three states and the third-nearest-neighbor hopping for the Hamiltonian $H_0^{(W)}$, the HHG calculations can break the laser-electromagnetic gauge symmetry.

The difference between both gauges compared to the TDDFT result can be explained by several factors, such as the incomplete sum rule between the position and the momentum operator in Eq. (D1) of Appendix D. The incomplete basis set of TBA breaks this commutation relation and therefore breaks the electromagnetic gauge symmetry. For solids described in plane-wave basis, it has been proven that the VG requires up to the 30th band to obtain convergence [24], while the LG needs up to the 2nd band for convergence. Another origin of the difference between the VG and the LG results is the action of the dephasing time T_2 in $\hat{\rho}(\mathbf{k}, t)$. This phenomenological variable plays a different role in the two gauges (for details, see Appendix C). However, it is worth noting that the difference that comes from the sum rule is not dominant in high-order terms. The error in VG can be written as additional terms with the powers of $\mathbf{A}(t)$ [37,44], and becomes negligible in high order when a laser satisfies $|\mathbf{A}(t)| < 1$ a.u.. There are other papers that also observe big differences in low order but smaller differences in high order [24,31]. Since our interest is focused on the plateau region, we can expect qualitative agreement even without the exact sum rule. As a result, our HHG spectra show a similar trend in both gauges; for example, the plateau structure and cutoff are similar in the VG and LG SBEs (see Fig. 3).

B. Nonlinear optical response in topological materials: The velocity gauge

Next, we applied the VG SBEs to topological materials. The Haldane model belongs to the first class of topological Chern insulators (CIs). We used the topological Haldane model to study nonlinear optical emissions and charge currents induced by the laser-CI interactions. This prototype of CI will test our VG SBEs in topological materials by comparing our HHG simulations in the VG with those in the LG.

The total HHG spectra produced by a linearly polarized MIR laser for the LG and VG SBEs are shown in Fig. 4. We find qualitatively a good agreement between the HHG spectrum produced by the VG and LG SBEs. Surprisingly, the VG SBEs can reproduce the key features of HHG in topological materials even in this two-band toy model. In particular, the selection rules produced by the VG SBEs for the HOs in (i) the perturbative region (low HOs of the HHG-spectra), (ii) the plateau (middle part of the HHG spectra), and (iii) the cutoff (HO beyond which the intensities of subsequent HO drastically decrease) show good agreement with results from the LG [see Figs. 5(a) and 5(b)].

In Fig. 5, a detailed comparison is made between the HHG spectra in the VG and LG SBEs. Since both time-reversal symmetry and inversion symmetry are broken in the Haldane model, both even harmonics and odd harmonics can be seen in the HHG spectrum [19] along directions both perpendicular and parallel to laser polarization. This result is gauge symmetric, appearing both in the LG and the VG SBEs, as can be seen in Figs. 5(a) and 5(b).

Another interesting test for the VG SBEs is the calculation of the circular dichroism (CD). Reference [14] demonstrated that CD is a direct clue for the topological invariant as it changes with Chern number. We define the circular dichroism (CD) at HO l as the normalized intensity difference between HO l from the left circularly polarized laser (LCP) and the right circularly polarized laser (RCP),

$$\mathrm{CD}_l = \frac{I_{\mathrm{RCP}}^l - I_{\mathrm{LCP}}^l}{I_{\mathrm{RCP}}^l + I_{\mathrm{LCP}}^l}. \tag{14}$$
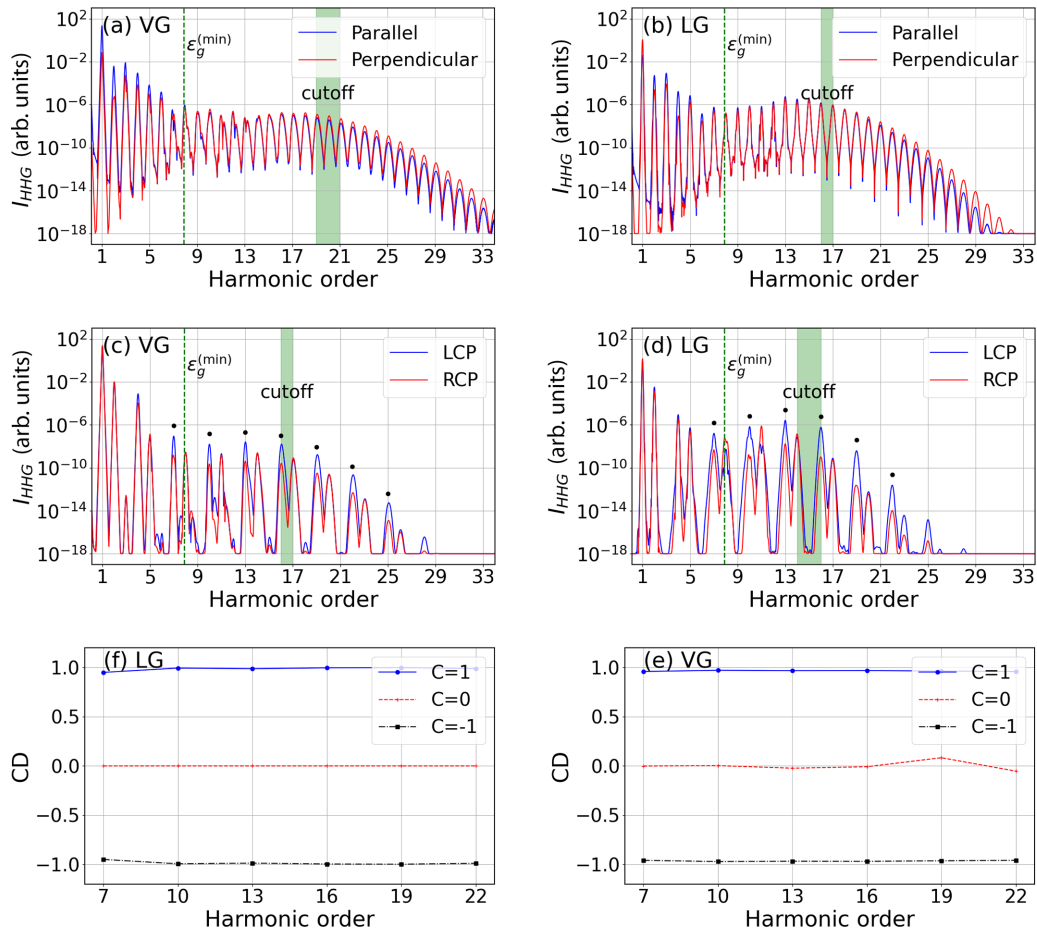
FIG. 5. Selection rules of the HHG spectra for the VG and LG in Chern insulators. [(a),(b)] Calculated HHG spectrums using linearly-polarized laser along Γ-K direction. Harmonic spectra along parallel or perpendicular direction relative to laser polarization are illustrated. [(c),(d)] Total harmonic spectras, $I_{\mathrm{HHG}}(\omega) = \omega(|J_x(\omega)|^2 + |J_y(\omega)|^2)$, produced by circularly-polarized lasers. Results from the right-hand/left-hand circularly-polarized laser (RCP/LCP) are shown. [(e),(f)] Circular dichroisms of the HHG spectra for each harmonic orders. Results from topologically trivial ($C = 0$) and nontrivial ($C = \pm 1$) are shown for each gauge. We use laser parameters of central frequency $\hbar\omega_0 = 0.38$ eV, peak electric field $E_0 = 0.0045$ a.u. and duration of 14 opt. cycles (in full width at half maximum) under a gaussian envelope. $T_2 = 5.3$ fs dephasing time is used. The cutoffs of the HHG spectra are on green shadows. The black dots indicate co-rotating harmonics for the calculation of CD. The vertical dashed lines show the bandgap of the topological material.

Figures 5(c) and 5(d) show the HHG spectra produced by the VG and LG SBEs. The co-rotating HOs, $l = 3n + 1$, produced by LCP are much larger than the corotating HOs produced by the RCP driver. We observe that for all corotating HOs, the CD = −1, for Haldane model parameters with $\nu = -1$. The correspondence between CD and Chern number is more obvious in Figs. 5(e)–5(f). The CDs of corotating orders are plotted for topological nontrivial material ($C = \pm 1$, Haldane model) and trivial material ($C = 0$). Apparently, CD follows the Chern number of the material and acts as a clue of the topological invariance. This is observed for both the VG and LG pictures, and is consistent with the previous report [14].

We now check whether the cutoff linear scaling law of the HHG spectrum can be verified within the VG SBEs [28]. The HHG spectra as a function of the electric field peak strength are shown in Fig. 6. Both the VG and LG show a similar linear cutoff law: the cutoff of HHG spectra increases linearly as the electric field strength E_0 increases with a similar slope. Finally, we show how the

occupation of the conduction band changes in time in Fig. 7 around $k_y = 0$.

IV. CONCLUSIONS

We discussed the laser-electromagnetic VG approach to overcome the singularity encountered in HHG calculation in topological materials. Using a two-band Haldane model, we show that the VG approach can qualitatively capture the main feature of charge current and the HHG spectra without any artificial noise introduced by the singularity of the dipole transition matrix elements, or Berry connection.

Additionally, we compare the HHG spectra in the VG approach with those produced by the LG in the maximally localized Wannier basis in terms of (1) the HHG spectra produced from linearly and circularly polarized lasers, (2) the circular dichroism, and (3) the linear cutoff law. In both trivial and topological materials, a good qualitative agreement was observed in the HHG spectrum between the VG and LG results. The lack of quantitative agreement between the two
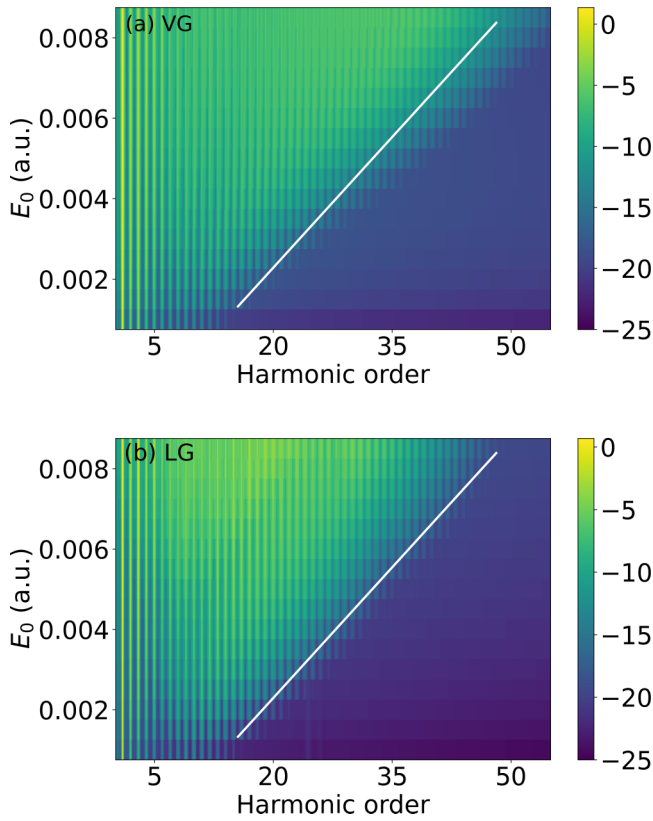
FIG. 6. Cutoff law for Chern insulators in both velocity and length gauges. Total HHG emissions, $I_{HHG}(\omega) = \omega(|J_x(\omega)|^2 + |J_y(\omega)|^2)$ as a function of electric field peak strength E_0 for (a) VG and (b) LG for linearly polarized light. Other laser parameters are the same as in Fig. 5. Both velocity and length gauges show linear scaling of the high harmonic cutoff with peak electric field.
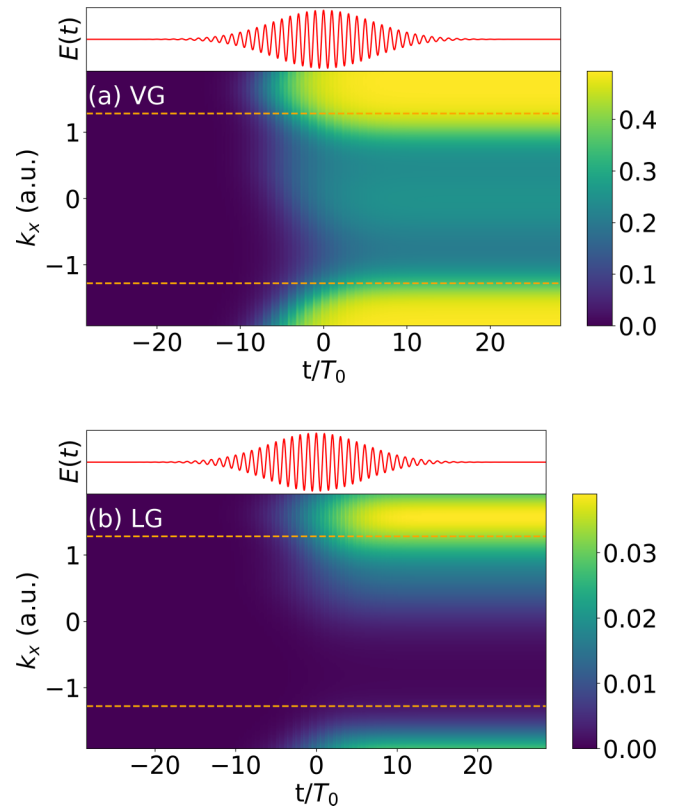

FIG. 7. Time-evolution of the "cross section" in the conduction band occupation. Occupation integrated along k_y is shown as a function of time. The k_x axis is along $K' - \Gamma - K$ direction (see Fig. 9), and the orange-dotted line indicates the K and K' point in the Brillouin zone.

approaches is partly due to the limited number of bands and the tight-binding approximation, which we used as a proof of concept.

In conclusion, we demonstrated that the VG approach can successfully integrate the numerical singularity in the Berry connection of topological materials and reproduce key features of the HHG spectrum in trivial materials as well as in nontrivial materials. We expect the VG approach to be more rigorous for topological materials, since it treats the numerical singularity present within the LG approach. Hence, the VG approach presented here introduces theoretical tools for investigating the highly nonlinear optical emission from topological materials.

APPENDIX A: THE HALDANE MODEL

The Haldane model [13] is the first model representing the quantum anomalous Hall effect (QAHE) introducing local magnetic flux. This model is a minimum of a two-band toy model but captures the most relevant physics of the Chern insulator. The Haldane model considers a TBA Hamiltonian in a hexagonal lattice and hopping parameters up to the next-nearest neighborhood (NNN).

This model can be a Chern insulator or a trivial insulator, depending on its parameter.

1. Haldane's Hamiltonian

The Haldane model is a two-band approximation obtained from a hexagonal lattice of two sublattices with atoms A and B. Thus, after applying the TBA for on-site potentials, the nearest-neighbor (NN) and the next-to-nearest-neighbor (NNN) interaction, and changing the Hamiltonian elements
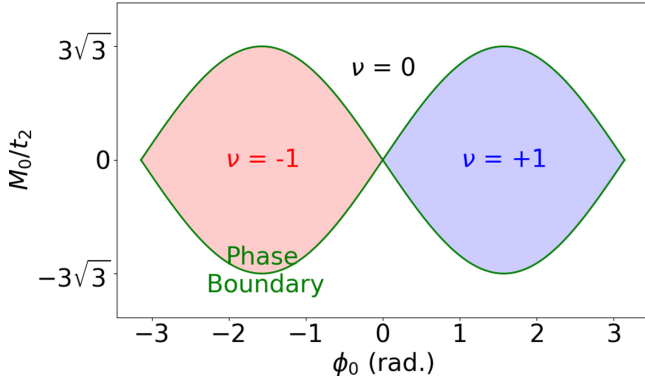
FIG. 8. Topological phase diagram for the Haldane model. The diagram shows three different topological phases $\nu = \{0, \pm 1\}$, where $\nu = 0$ indicates topologically trivial state and $\nu = \pm 1$ represents Chern insulator.

from Wannier function to Bloch basis, we find

$$H_0(\boldsymbol{k}) = B_0(\boldsymbol{k})I + \boldsymbol{B}(\boldsymbol{k}) \cdot \boldsymbol{\sigma}, \qquad (A1)$$

where I is the identity matrix and $\boldsymbol{\sigma} = \{\sigma_x, \sigma_y, \sigma_z\}$ are Pauli matrices. Additionally, the $\boldsymbol{B}(\boldsymbol{k}) = \{B_1(\boldsymbol{k}), B_2(\boldsymbol{k}), B_3(\boldsymbol{k})\}$ is known as pseudomagnetic field. Each vector is

$$B_0(\boldsymbol{k}) = 2t_2 \cos\phi_0 \sum_{i=1}^{3} \cos(\boldsymbol{k} \cdot \boldsymbol{b}_i), \qquad (A2)$$

$$B_1(\boldsymbol{k}) = t_1 \sum_{i=1}^{3} \cos(\boldsymbol{k} \cdot \boldsymbol{a}_i), \qquad (A3)$$

$$B_2(\boldsymbol{k}) = t_1 \sum_{i=1}^{3} \sin(\boldsymbol{k} \cdot \boldsymbol{a}_i), \qquad (A4)$$

$$B_3(\boldsymbol{k}) = M_0 - 2t_2 \sin\phi_0 \sum_{i=1}^{3} \sin(\boldsymbol{k} \cdot \boldsymbol{b}_i), \qquad (A5)$$

where t_1 is the NN hopping parameter and t_2 is the NNN hopping parameter. M_0 is on-site potential that breaks the inversion symmetry and ϕ_0 the local magnetic flux, which breaks the time-reversal symmetry. $\boldsymbol{a}_i$ are the NN vectors, and $\boldsymbol{b}_i$ the NNN vectors.

The displacement vectors are given by $\mathbf{a}_1 = (0, a_0)$, $\mathbf{a}_2 = \frac{1}{2}(-\sqrt{3}, -1)a_0$, $\mathbf{a}_3 = \frac{1}{2}(\sqrt{3}, -1)a_0$, $\mathbf{b}_1 = (\sqrt{3}, 0)a_0$, $\mathbf{b}_2 = \frac{1}{2}(-\sqrt{3}, +3)a_0$, and $\mathbf{b}_3 = \frac{1}{2}(-\sqrt{3}, -3)a_0$.

Figure 8 shows the topological phase diagram of Haldane model. The Haldane model yields a gapless band structure, where the topological phase transition occurs, with the condition $M_0/t_2 = \pm 3\sqrt{3} \sin\phi_0$.

Haldane model can have three topological invariants or Chern numbers or topological phases $\nu = \{-1, 0, +1\}$, where $\nu = 0$ is a trivial insulator (or "Dirac semimetal") and $\nu = \pm 1$ is a topological nontrivial phase.

As shown in Fig. 8, the topological phase is determined by ϕ_0 and M_0/t_2. t_1 affects band structure but does not affect the topological phase. By controlling these parameters, we can adjust the bandgap and topological phase to mimic a topological CI.
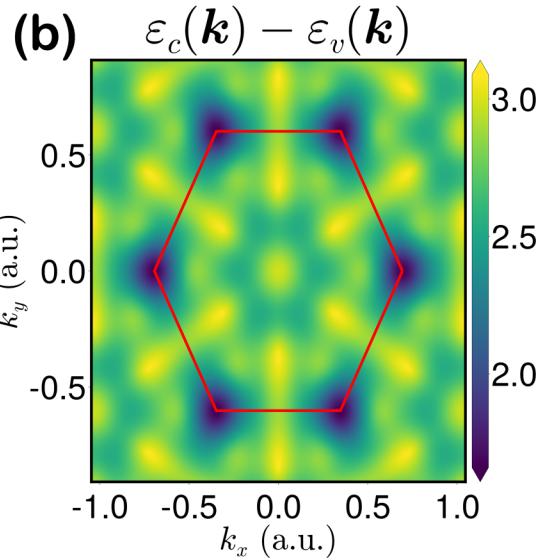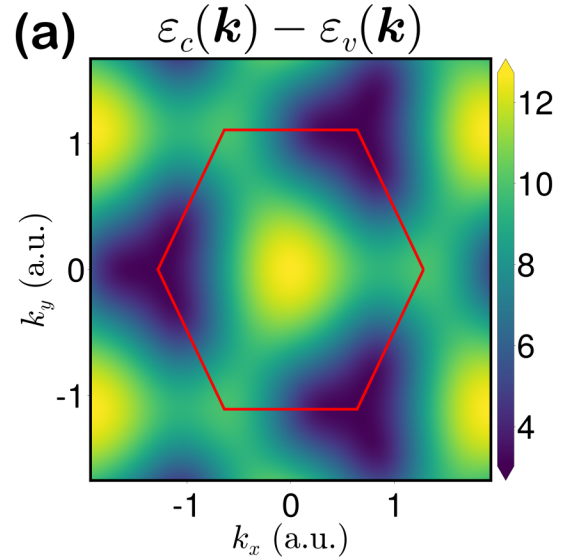

FIG. 9. Energy dispersion for the model used in calculation. Band gap (eV) for (a) a Chern insulator from the Haldane model and (b) a trivial material, MoS$_2$. As time-reversal symmetry is broken, (a) shows different bandgap in the K' and K point while (b) has the same bandgap.

2. Dipoles, Berry connection, Berry curvature and Chern number

Fortunately, we can solve the 2x2 Hamiltonian analytically. The energy dispersion of the Haldane model reads

$$\varepsilon_{c/v}(\boldsymbol{k}) = B_0(\boldsymbol{k}) \pm |\boldsymbol{B}(\boldsymbol{k})|. \qquad (A6)$$

The band gap for Haldane model is shown in Fig. 9. In Fig. 9(a) we show that band gap at K and K' is different for Chern insulator. In contrast, there is no difference between band gap at K and K' for MoS$_2$ as shown in Fig 9(b). Here we use parameters $M_0 = 0.0635$ a.u., $t_1 = 0.075$ a.u., $t_2 = 0.025$ a.u., and $\phi_0 = 1.16$ rad for topological material. For trivial material, MoS$_2$, $M_0 = 0.9$ eV $= 0.0331$ a.u., $t_1 = 0.4$ eV $= 0.0147$ a.u., $t_2 = 0.667$ eV $= 0.0245$ a.u., and $\phi_0 = 0$ are used.

To investigate topological aspects of materials, it is required to calculate the dipole matrix elements,

$$\mathbf{d}_{m'm}(\boldsymbol{k}) = i\langle u_{m',\boldsymbol{k}}|\nabla_{\boldsymbol{k}}|u_{m,\boldsymbol{k}}\rangle, \tag{A7}$$

where $|u_m\boldsymbol{k}\rangle$ is the periodic part of a Bloch state. Usually, people distinguish diagonal and off-diagonal components in Eq. (A7) and call diagonal components Berry connections,

$$\boldsymbol{\xi}_m(\mathbf{k}) = \mathbf{d}_{mm}(\boldsymbol{k})$$
$$= i\langle u_{m,\boldsymbol{k}}|\nabla_{\boldsymbol{k}}|u_{m,\boldsymbol{k}}\rangle. \tag{A8}$$

The Berry connection and the dipole matrix elements are plotted in Figs. 2 and 10. The dipole matrix element shows an interesting vortex structure in topological phases, which might lead to a totally different coupling with the linearly and elliptically polarized lasers [see K' points in Fig. 10(a) vs Fig. 10(b)].

The Berry connection has singularity while the off-diagonal dipole "only has discontinuity" [see Fig. 2(a)]. Moreover, the dipole absolute value is gauge invariant and has no discontinuity [see Fig. 10(a)]. Although the Berry connection is wavefunction gauge dependent, the curl of the Berry connection, named the Berry curvature,

$$\boldsymbol{\Omega}_m(\mathbf{k}) = \nabla_{\boldsymbol{k}} \times \boldsymbol{\xi}_m(\mathbf{k}) \tag{A9}$$

is gauge invariant. The integration of the Berry curvature over the Brillouin zone,

$$\nu_m := \frac{1}{2\pi} \int_{\text{BZ}} \boldsymbol{\Omega}_m(\mathbf{k}) \cdot d^2\mathbf{k}, \tag{A10}$$

is a *topological invariant* of the system, called Chern number, which is shown in Fig. 8.

APPENDIX B: HHG SPECTRA WITHOUT INTEGRATING SINGULARITY

In Fig. 11, we show the HHG spectra from the Chern insulator with a linearly-polarized laser along the $\Gamma - K$ direction. Calculation is done by the LG SBEs without singularity treatment, the VG SBEs, and the LG SBEs with Wannier representation. The data for noisy LG HHG spectra are taken from previous paper [14]. The LG SBEs result without singularity treatment shows a noisy spectrum and a wrong cutoff, while the other two results match qualitatively.

APPENDIX C: EFFECTS OF DEPHASING IN LENGTH AND VELOCITY GAUGES

This Appendix numerically studies the effects of the dephasing T_2 on the HHG process for our topological Chern insulator.

The phenomenological dephasing time T_2 can be considered as an external term related to the scattering and thermal processes in a medium, and therefore gives the same effect on the LG and VG. However, from a numerical point of view, T_2 acts differently in both electromagnetic gauges [24,45]. This is the primary source of discrepancies in breaking laser-electromagnetic gauge symmetry. To avoid this T_2 effect, one can apply T_2 only in the LG picture even if we use the VG SBEs. This can be done as follows: convert the VG density matrix to the LG density matrix, apply the dephasing time, and
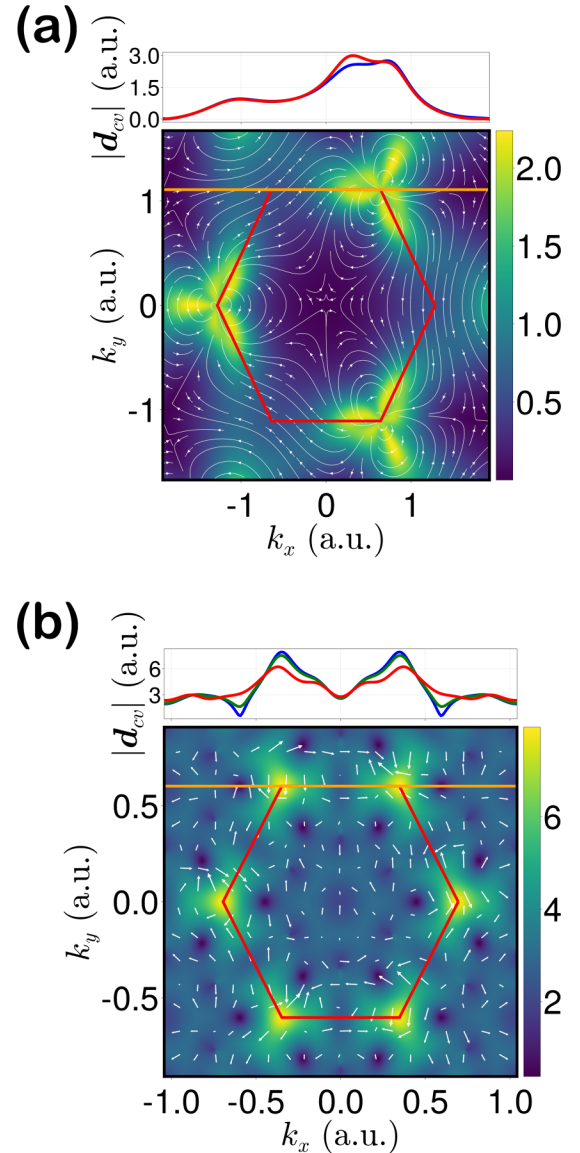

(a)

(b)

FIG. 10. Dipole matrix element for topological materials. Absolute value of the dipole matrix element for (a) a Chern insulators defined in the topological Haldane model and (b) a topologically trivial material, i.e., MoS$_2$. The vectorial field indicates real components of the dipole matrix element. The upper panels show it cut along the orange line, i.e., the real value of dipole is plotted along the orange line with small k_y offsets. The absolute value of the dipole is smooth for both cases, but the nontrivial topological case (a) has a vortex while (b) has no discontinuity.

return to the VG density matrix [24]. However, this procedure slows down the calculation speed of the HHG spectra in VG. Therefore, we do not use this transformation and show that important features are preserved even without additional treatment for T_2. We get an increased number of computational operations and the longer time spent on this calculation. For this case, the VG SBEs can be even slower than the LG SBEs. Nevertheless, when the VG SBEs is compared to Wannier basis SBEs, VG still has its advantage since Wannier LG also needs transformation to apply T_2.
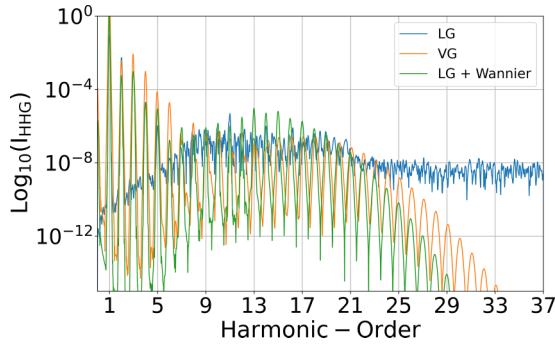
FIG. 11. Calculated HHG spectra from Chern insulator in the velocity gauge, length gauge with or without integrating singularity. Noisy spectrum data comes from previous paper [14]. Parameters are the same as Fig. 3.

In Figs. 12(a) and 12(b) we represent the HHG spectra with different dephasing times T_2 for a topological Chern insulator (CI). In the perturbative region of the HHG spectra ([1st, 6th]), HOs show different tendencies between two gauges. Significantly, in the LG SBEs, the harmonic yield increases while the T_2 decreases for low HOs [22]. In contrast, we find that the VG SBEs provides a behavior opposite to that of the LG SBEs for low orders as a function of T_2.

For the plateau and cutoff regions of the HHG spectra, the dephasing time T_2 also induces a symmetry gauge break
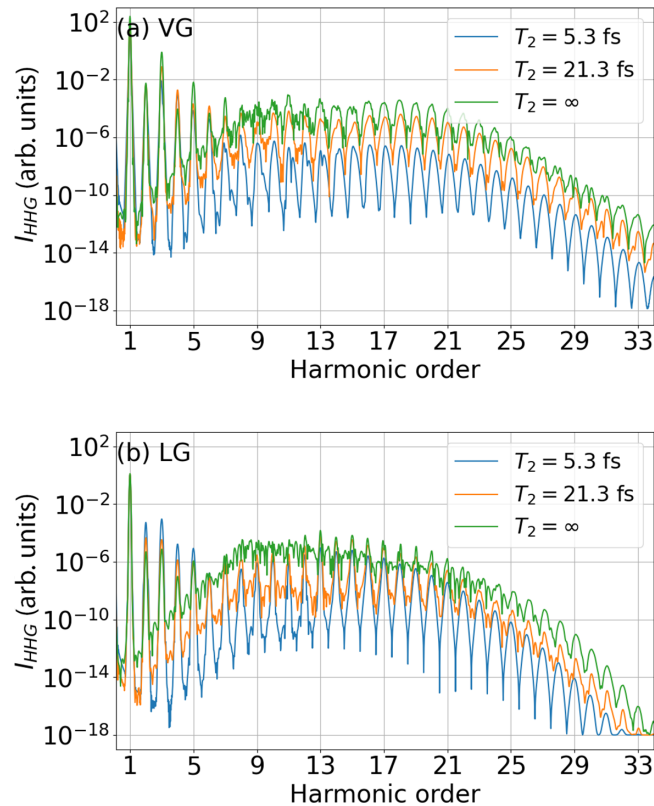

FIG. 12. Effect of T_2 for Chern insulator in LG and VG. HHG calculation results for (a) VG and (b) LG. The laser is linearly polarized along the $\Gamma - K$ direction, and the laser parameters of Fig. 5 are used.
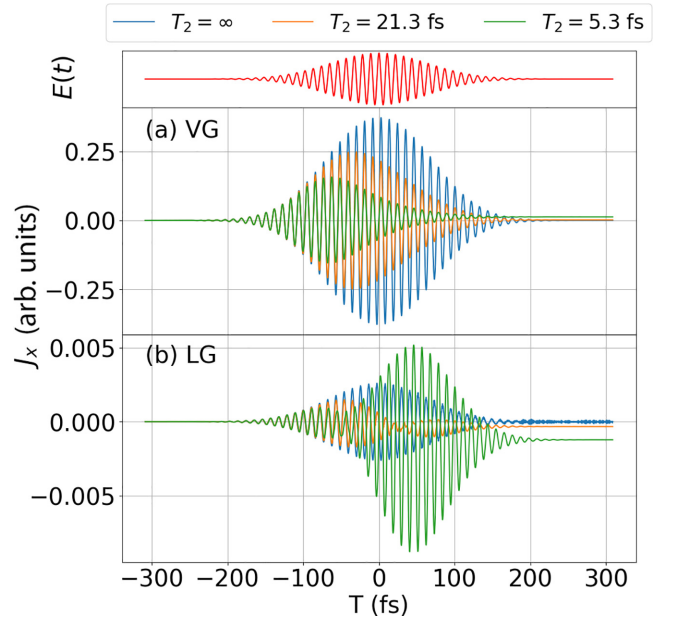

FIG. 13. Effect of T_2 for Chern insulator in length gauge and velocity gauge in current. Total current for (a) velocity gauge and (b) length gauge. All the parameters are the same as Fig. 12.

in the HHG spectrum. Nevertheless, it is difficult to quantify the difference between two gauges in Fig. 12, since T_2 reduce the noise in the both gauges. It is more obvious to observe the differences through current.

Figure 13 illustrates the effect of T_2 on currents as a function of time. For the VG, they act like a window function that removes the contribution from the later time domain. For the LG, the effect is more complex and global. The noise at $T_2 = \infty$ is filtered, and the shape of the envelope is also changed.

1. Computational complexities

We give a brief illustration of the computational cost for each method. In the case of LG SBEs, there are several choices like a gradient or moving frame, but here we only mention the moving frame with a tight-binding model. For both LG and VG SBEs, they have to calculate SBEs by matrix multiplication and addition, and it costs about $f_{SBEs} = O(N_k N_b^3)$ by setting matrix multiplication cost as $O(N_b^3)$. Here, N_k is the total number of k-space grids and N_b is the number of bands. LG SBEs have to calculate matrix elements at $\boldsymbol{K} + \boldsymbol{A}(t)$ for each time step. Then it needs $f_{GenMatrix} = O(N_k N_b^2)$ order to generate appropriate matrices when we assume that the run time for calculating each component is $O(1)$. Then the computation complexity for LG and VG SBEs without dephasing time is

$$f_{LG} = f_{SBEs} + f_{GenMatrix}, \tag{C1}$$

$$f_{VG}^{nodeph} = f_{SBEs}. \tag{C2}$$

If we include the dephasing time, LG SBEs have almost no additional cost, but Wannier LG SBEs and VG have a conversion cost of about $f_{dephasing} = O(N_k N_b^3)$, which includes

generating an eigenvector matrix and multiplying this. The direct cost of the dephasing time in VG and Wannier LG is slightly different, but the difference is small enough to be ignored. Then the computational cost for Wannier or VG is

$$f_{\text{LG}}^{(W)} = f_{\text{SBEs}} + f_{\text{GenMatrix}} + f_{\text{dephasing}}, \tag{C3}$$

$$f_{\text{VG}} = f_{\text{SBEs}} + f_{\text{dephasing}}. \tag{C4}$$

As an example, in the calculation of Fig. 4, VG uses around 17 hours of CPU time, while Wannier needs about 64 hours. There might be an additional source of computational time difference, such as cache-miss. This kind of optimization problem affects LG mainly, since the implementation of VG is more straightforward.

APPENDIX D: GAUGE COVARIANCE

1. Sum rule for gauge covariance

It is well known that VG needs more bands to get convergence with LG. The main problem is the canonical commutation relation

$$[\hat{x}^{\alpha}, \hat{p}^{\beta}] = i\delta_{\alpha\beta}, \tag{D1}$$

where $\{\alpha, \beta\} = \{x, y, z\}$, is generally not valid when we have finite bands [29–31,37].

In the plane-wave basis, we can numerically satisfy this relation by increasing the number of bands up to the convergence, but it needs a large number of bands. For example, in the case of hBN, VG needs up to 30 bands to match the LG calculation of 2 bands [24]. However, in TBA, situation is more complex that we cannot state that more bands always give better results given for the given constraint of Eq. (D1).

With the quantum Liouville equation, a velocity operator can be expressed as $\hat{v} = -i[\hat{x}, \hat{H}]$. A position operator in Bloch-like basis is written as $\hat{x} = i\frac{\partial}{\partial k} + \hat{D}$ [37,38]. Then, the momentum matrix reads

$$\hat{P} = \frac{\partial \hat{H}_0}{\partial \boldsymbol{k}} - i[\hat{D}, \hat{H}_0]. \tag{D2}$$

If we use the Hamiltonian gauge, H_0 becomes a diagonal matrix of energy dispersion [40,46]. Then, Eq. (D2) becomes the well-known formula [37,40]

$$\boldsymbol{P}_{mn} = \begin{cases} \frac{\partial}{\partial \boldsymbol{k}}\varepsilon_m & \text{if } m = n, \\ i(\varepsilon_m - \varepsilon_n)\boldsymbol{d}_{mn} & \text{if } m \neq n \end{cases}, \tag{D3}$$

in which the first term is the intraband component, and other terms define the interband currents.

In the Wannier representation, H_0 is modeled by the TBA, which implies

$$\boldsymbol{P} = \frac{\partial H_0}{\partial \boldsymbol{k}} - i[\boldsymbol{D}^{(W)}(\boldsymbol{k}), H_0(\boldsymbol{k})]. \tag{D4}$$

Using Eq. (D4), Eq. (D1) becomes the sum rule,

$$i\delta_{\alpha\beta}I = i\frac{\partial^2 \hat{H}_0}{\partial k_\alpha \partial k_\beta} + \frac{\partial}{\partial k_\alpha}[\hat{D}^\beta, \hat{H}_0]$$
$$+ \left[\hat{D}^\alpha, \frac{\partial \hat{H}_0}{\partial k_\beta}\right] + i[[\hat{D}^\beta, \hat{H}_0], \hat{D}^\alpha]. \tag{D5}$$

If we use the condition $D^{(W)}(\boldsymbol{k}) = \boldsymbol{0}$ [which is just another representation of Eq. (13) with basis transformation], the sum rule in Wannier representation becomes

$$\delta_{\alpha\beta}I = \frac{\partial^2 H_0}{\partial k_\alpha \partial k_\beta}, \tag{D6}$$

which is only valid when $H_{mn} \approx \frac{1}{2}k^2\delta_{mn} + O(k)$. In plane-wave basis, we can reach the numerical convergence by increasing the number of bands since the central equation of the Bloch function in plane-wave basis naturally satisfies the above condition. However, in TBA, it is almost impossible to match such a condition. This shows that the diagonal approximation in Eq. (13) is not sufficient to match the sum rule.

2. Conversion between electromagnetic gauges

We can convert the operators between two gauges as [37]

$$\hat{O}^{(\text{VG})}(\boldsymbol{k}) = \hat{O}^{(\text{LG})}(\boldsymbol{k} + \boldsymbol{A}(t)). \tag{D7}$$

However, the form of the operator $\hat{O}^{(\text{VG})}(\boldsymbol{k})$ is straightforward; the matrix form of the relationship between the density matrices of the VG and LG is complicated [24,45].

$$\hat{O}^{(\text{LG})}(\boldsymbol{k} + \boldsymbol{A}) = R(\boldsymbol{k}, \boldsymbol{A})\hat{O}^{(\text{VG})}(\boldsymbol{k})R^\dagger(\boldsymbol{k}, \boldsymbol{A}), \tag{D8a}$$

$$R_{mn}(\boldsymbol{k}, \boldsymbol{A}) \equiv \langle u_{m\boldsymbol{k}+\boldsymbol{A}}|u_{n\boldsymbol{k}}\rangle. \tag{D8b}$$

In TBA, Eq. (D8) can be calculated by

$$R^{\boldsymbol{k}, \boldsymbol{A}} = \hat{U}^{\boldsymbol{k}+\boldsymbol{A}\dagger}\hat{U}^{\boldsymbol{k}}, \tag{D9}$$

where $\hat{U}^{\boldsymbol{k}}$ is the unitary eigenvector matrix of the unperturbed Hamiltonian $\hat{H}_0$.

[1] M. König, S. Wiedmann, C. Brüne, A. Roth, H. Buhmann, L. W. Molenkamp, X.-L. Qi, and S.-C. Zhang, Science **318**, 766 (2007).

[2] B. A. Bernevig, T. L. Hughes, and S.-C. Zhang, Science **314**, 1757 (2006).

[3] H. Zhang, C.-X. Liu, X.-L. Qi, X. Dai, Z. Fang, and S.-C. Zhang, Nat. Phys. **5**, 438 (2009).

[4] Y. L. Chen, J. G. Analytis, J.-H. Chu, Z. K. Liu, S.-K. Mo, X. L. Qi, H. J. Zhang, D. H. Lu, X. Dai, Z. Fang *et al.*, Science **325**, 178 (2009).

[5] S. A. Oliaei Motlagh, J. S. Wu, V. Apalkov, and M. I. Stockman, Phys. Rev. B **98**, 125410 (2018).

[6] M. Z. Hasan and C. L. Kane, Rev. Mod. Phys. **82**, 3045 (2010).

[7] X. L. Qi and S. C. Zhang, Rev. Mod. Phys. **83**, 1057 (2011).

[8] D. Xiao, M. C. Chang, and Q. Niu, Rev. Mod. Phys. **82**, 1959 (2010).

[9] D. Haddad, F. Seifert, L. S. Chao, S. Li, D. B. Newell, J. R. Pratt, C. Williams, and S. Schlamminger, Rev. Sci. Instrum. **87**, 061301 (2016).

[10] H.-H. Kung, A. P. Goyal, D. L. Maslov, X. Wang, A. Lee, A. F. Kemper, S.-W. Cheong, and G. Blumberg, Proc. Natl. Acad. Sci. USA **116**, 4006 (2019).

[11] C. L. Kane and E. J. Mele, Phys. Rev. Lett. **95**, 226801 (2005).

[12] D. Shin, S. A. Sato, H. Hübener, U. De Giovannini, J. Kim, N. Park, and A. Rubio, Proc. Natl. Acad. Sci. USA **116**, 4135 (2019).

[13] F. D. M. Haldane, Phys. Rev. Lett. **61**, 2015 (1988).

[14] A. Chacón, D. Kim, W. Zhu, S. P. Kelly, A. Dauphin, E. Pisanty, A. S. Maxwell, A. Picón, M. F. Ciappina, D. E. Kim, C. Ticknor, A. Saxena, and M. Lewenstein, Phys. Rev. B **102**, 134115 (2020).

[15] J. M. Kosterlitz, Rev. Mod. Phys. **89**, 040501 (2017).

[16] M. Kohmoto, Ann. Phys. **160**, 343 (1985).

[17] D. Bauer and K. K. Hansen, Phys. Rev. Lett. **120**, 177401 (2018).

[18] H. Drüeke and D. Bauer, Phys. Rev. A **99**, 053402 (2019).

[19] D. Baykusheva, A. Chacón, D. Kim, D. E. Kim, D. A. Reis, and S. Ghimire, Phys. Rev. A **103**, 023101 (2021).

[20] J. W. McIver, B. Schulte, F.-U. Stein, T. Matsuyama, G. Jotzu, G. Meier, and A. Cavalleri, Nat. Phys. **16**, 38 (2020).

[21] R. E. F. Silva, B. Amorim, O. Smirnova, M. Ivanov, A. Jiménez-Galán, B. Amorim, O. Smirnova, and M. Ivanov, Nat. Photonics **13**, 849 (2019).

[22] G. Vampa, C. R. McDonald, G. Orlando, D. D. Klug, P. B. Corkum, and T. Brabec, Phys. Rev. Lett. **113**, 073901 (2014).

[23] F. Bloch, Phys. Rev. **70**, 460 (1946).

[24] L. Yue and M. B. Gaarde, Phys. Rev. A **101**, 053411 (2020).

[25] C. Liu, Y. Zheng, Z. Zeng, and R. Li, New J. Phys. **22**, 073046 (2020).

[26] M. S. Mrudul and G. Dixit, Phys. Rev. B **103**, 094308 (2021).

[27] R. E. F. Silva, F. Martín, and M. Ivanov, Phys. Rev. B **100**, 195201 (2019).

[28] S. Ghimire, A. D. DiChiara, E. Sistrunk, P. Agostini, L. F. DiMauro, and D. A. Reis, Nat. Phys. **7**, 138 (2011).

[29] K. S. Virk and J. E. Sipe, Phys. Rev. B **76**, 035213 (2007).

[30] S. Y. Kruchinin, M. Korbman, and V. S. Yakovlev, Phys. Rev. B **87**, 115201 (2013).

[31] V. S. Yakovlev and M. S. Wismer, Comput. Phys. Commun. **217**, 82 (2017).

[32] C. Granados and L. Plaja, Phys. Rev. A **85**, 053403 (2012).

[33] J. A. Pérez-Hernández, L. Roso, and L. Plaja, Laser Phys. **19**, 1581 (2009).

[34] A. Chacón, M. F. Ciappina, and M. Lewenstein, Phys. Rev. A **92**, 063834 (2015).

[35] E. Cormier and P. Lambropoulos, J. Phys. B: At., Mol. Opt. Phys. **29**, 1667 (1996).

[36] K. Amini, J. Biegert, F. Calegari, A. Chacón, M. F. Ciappina, A. Dauphin, D. K. Efimov, C. F. de Morisson Faria, K. Giergiel, P. Gniewek *et al.*, Rep. Prog. Phys. **82**, 116001 (2019).

[37] G. B. Ventura, D. J. Passos, J. M. Lopes Dos Santos, J. M. Viana Parente Lopes, and N. M. Peres, Phys. Rev. B **96**, 035431 (2017).

[38] E. Blount, in *Solid State Physics*, edited by F. Seitz and D. Turnbull, Vol. 13 (Academic Press, New York, 1962), pp. 305–373.

[39] G. Vampa and T. Brabec, J. Phys. B: At. Mol. Opt. Phys. **50**, 083001 (2017).

[40] X. Wang, J. R. Yates, I. Souza, and D. Vanderbilt, Phys. Rev. B **74**, 195118 (2006).

[41] N. Tancogne-Dejean, M. J. T. Oliveira, X. Andrade, H. Appel, C. H. Borca, G. Le Breton, F. Buchholz, A. Castro, S. Corni, A. A. Correa *et al.*, J. Chem. Phys. **152**, 124119 (2020).

[42] G. B. Liu, W. Y. Shan, Y. Yao, W. Yao, and D. Xiao, Phys. Rev. B **88**, 085433 (2013).

[43] Y. C. Han and L. B. Madsen, Phys. Rev. A **81**, 063430 (2010).

[44] C. Aversa and J. E. Sipe, Phys. Rev. B **52**, 14636 (1995).

[45] G. Ernotte, T. J. Hammond, and M. Taucer, Phys. Rev. B **98**, 235202 (2018).

[46] N. Marzari and D. Vanderbilt, Phys. Rev. B **56**, 12847 (1997).